RITG142

THE SINGLE-VENDOR SOFTWARE SOLUTION FOR EVERY QA TEST RECOMMENDED IN TG-142

Perform comprehensive quality assurance of linear accelerators with confidence and ease, using an EPID and RIT software. Use either RITG142 or RIT *Complete* as your all-in-one software product for Machine QA, MLC QA, Imaging QA, and all the data tracking and trending you need to be in compliance with TG-142.

Daily, Monthly & Annual LINAC Machine QA Tests

- Enhanced 3D Winston-Lutz (Isocenter Optimization)
- RIT's New Fully-Automated Star Shot Analysis
- Stereotactic Alignment (2D Winston-Lutz) Test
- Radiation/Light Field Coincidence
- Stereotactic Cone Profiles
- Field Alignment Test
- Electron Energy (TG-25)
- Asymmetric Field/Matchline
- Quick Flatness and Symmetry
- Water Tank Beam Measurement Analysis
- Depth Dose Profiles, Cross Profiles & Orthogonal Profiles

Fast and Easy Quantitative MLC QA

- EPID Picket Fence Test
- Leaf Speed Tests for Varian and Elekta
- Hancock Tests for Elekta Machines
- Automated Varian RapidArc® Tests (0.1, 0.2, 0.2 HD, 1.1, 1.1 HD, 1.2, 1.2 HD, 2 and 3)
- Bayouth MLC Test
- TG-50 Picket Fence Test
- MSK Leaf Test
- Varian DMLC Test Patterns
- MLC Transmission Analysis

One-Click Instant Imaging QA

- **Planar MV (EPID) Imager:** EPID phantom, Las Vegas, PTW EPID QC, and Standard Imaging QC-3 Phantoms
- **Planar kV Imaging:** IBA Primus® L, PTW NORMI®-4, Leeds TOR-18 FG, and Standard Imaging QC-kV1 Phantoms
- **CBCT/MVCT:** CATPHAN® 504 and 604 for Varian, CATPHAN® 503 Elekta XVI and Siemens MVCT Phantoms
- **Daily IGRT QA:** ISOCube™ Phantom kV-MV Isocenter Coincidence, CBCT Isocenter Coincidence, kV Collimation, MV Collimation/Light Field, and 6 Degree-of-Freedom Couch Tests

RIT software simplifies the process of creating a routine QA program at your facility, streamlines the reporting process for accreditation, and provides you with a better understanding of measurement performance across multiple machines and facilities.

SCHEDULE A PERSONAL DEMO OF RIT'S TG-142 CAPABILITIES TODAY!

RADIMAGE.COM®

+1.719.590.1077 x211 // sales@radimage.com // Connect with us on social media @RIT4QA

RIT

Three-dimensional MRI-based treatment planning approach for non-invasive ocular proton therapy

E. Fleury[a] (iD) and P. Trnková
Department of Radiation Oncology, Erasmus Medical Center, Rotterdam, The Netherlands
Department of Radiation Oncology, HollandPTC, Delft, The Netherlands

E. Erdal
Department of Radiation Oncology, HollandPTC, Delft, The Netherlands

M. Hassan, B. Stoel and M. Jaarma-Coes
Department of Radiology, Leiden University Medical Center, Leiden, The Netherlands

G. Luyten
Department of Ophthalmology, Leiden University Medical Center, Leiden, The Netherlands

J. Herault
Department of Radiation Oncology, Centre Antoine Lacassagne, Nice, France

A. Webb
Department of Radiology, Leiden University Medical Center, Leiden, The Netherlands

J.-W. Beenakker
Department of Radiology, Leiden University Medical Center, Leiden, The Netherlands
Department of Ophthalmology, Leiden University Medical Center, Leiden, The Netherlands

J.-P. Pignol
Department of Radiation Oncology, Dalhousie University, Halifax, Canada

M. Hoogeman
Department of Radiation Oncology, Erasmus Medical Center, Rotterdam, The Netherlands
Department of Radiation Oncology, HollandPTC, Delft, The Netherlands

Purpose: To develop a high-resolution three-dimensional (3D) magnetic resonance imaging (MRI)-based treatment planning approach for uveal melanomas (UM) in proton therapy.

Materials/methods: For eight patients with UM, a segmentation of the gross tumor volume (GTV) and organs-at-risk (OARs) was performed on T1- and T2-weighted 7 Tesla MRI image data to reconstruct the patient MR-eye. An extended contour was defined with a 2.5-mm isotropic margin derived from the GTV. A broad beam algorithm, which we have called πDose, was implemented to calculate relative proton absorbed doses to the ipsilateral OARs. Clinically favorable gazing angles of the treated eye were assessed by calculating a global weighted-sum objective function, which set penalties for OARs and extreme gazing angles. An optimizer, which we have named OPT'im-Eye-Tool, was developed to tune the parameters of the functions for sparing critical-OARs.

Results: In total, 441 gazing angles were simulated for every patient. Target coverage including margins was achieved in all the cases ($V_{95\%} > 95\%$). Over the whole gazing angles solutions space, maximum dose (D_{max}) to the optic nerve and the macula, and mean doses (D_{mean}) to the lens, the ciliary body and the sclera were calculated. A forward optimization was applied by OPT'im-Eye-Tool in three different prioritizations: iso-weighted, optic nerve prioritized, and macula prioritized. In each, the function values were depicted in a selection tool to select the optimal gazing angle(s). For example, patient 4 had a T2 equatorial tumor. The optimization applied for the straight gazing angle resulted in objective function values of 0.46 (iso-weighted situation), 0.90 (optic nerve prioritization) and 0.08 (macula prioritization) demonstrating the impact of that angle in different clinical approaches.

Conclusions: The feasibility and suitability of a 3D MRI-based treatment planning approach have been successfully tested on a cohort of eight patients diagnosed with UM. Moreover, a gaze-angle trade-off dose optimization with respect to OARs sparing has been developed. Further validation of the whole treatment process is the next step in the goal to achieve both a non-invasive and a personalized proton therapy treatment. *© 2020 The Authors. Medical Physics published by Wiley Periodicals LLC on behalf of American Association of Physicists in Medicine.* [https://doi.org/10.1002/mp.14665]

Key words: MRI, proton therapy, uveal melanoma

1. INTRODUCTION

Uveal melanoma (UM) originates mostly from the choroid and less frequently in the ciliary body and iris areas. Proton therapy for uveal melanoma is one of the main radiotherapy options for treating these malignant intraocular tumors,[1–12] enabling both improved dose distribution homogeneity and sharp dose gradients. Proton therapy is suitable for large and peri-papillary-/-macular uveal melanomas, and it is mostly delivered by dedicated passive scattering horizontal beamlines.[3,13]

The clinical workflow, including surgery for clips placement, in-room simulations and positioning, planning and treatment completions, has been described in detail by a wide spectrum of publications over the last four decades.[8,14–18] In short, patients undergo surgery prior to proton therapy, with clips stitched onto the sclera to outline the tumor boundary. The purpose of these invasive clips is twofold: first, to delineate the tumor volume within a geometrical-based eye model; second, to position and verify the correct gazing angle during treatment. For planning, a series of X-ray images of the eye are acquired at different gazing angles and imported into the treatment planning system (TPS) for the selection of the optimal eye model and target delineation. Subsequently, the optimal gazing angle of the eye for the treatment is defined by a manual rotation of the eye model around its center, and dose parameters are evaluated in a manual manner by a trade-off between target coverage and sparing of specific organs-at-risks (OARs). The optimal gazing angle selection can also be automated as demonstrated by the Paul Scherrer Institute team (PSI, Villigen, Switzerland).[19]

Manual and automatic treatment planning procedures are both currently limited by the lack of accurate 3D information for target and OARs definition. The Deutsches Krebsforschungszentrum (DKFZ, Heidelberg, Germany) in partnership with the Helmholtz-Zentrum in Berlin have developed OCTOPUS[20] (Ocular Tumour Planning UtilitieS) for integrating a more complex eye model definition. In this TPS, the eye model is interactively adapted to computed tomography (CT) or magnetic resonance imaging (MRI) datasets[21] and afterwards it is registered to the image data. Since diagnosis of uveal melanomas increasingly incorporates MRI information,[22–24] there is a need to develop MRI-based treatment planning. The MR-compatibility of tantalum clips, which are currently being used as landmarks, has been proved.[25] In addition, 3 and 7 Tesla high-resolution MRI sequences have been developed to enable improved UM and OARs delineation compared to conventional MRI procedures which do not clearly discriminate ocular structures.[26] The Paul Scherrer Institute is currently also investigating how MRI sequences can be used for improvement in the eye model definition.[27] This emerging imaging modality strengthens the justification to shift toward MRI for ocular proton therapy planning with the ultimate goal of providing a non-invasive, that is, clipless, ocular proton therapy treatment.

The aim of this project was to assess the feasibility of implementing a full 3D MRI-based treatment planning approach with a gaze-angle proton dose optimization from 7 Tesla high-resolution MRI data. To our knowledge, currently no system incorporates these two cutting-edge approaches, MRI-based delineation and automatic treatment planning, into one dedicated platform.

2. MATERIALS AND METHODS

2.A. Outline

The 3D MRI-based ocular proton therapy treatment planning approach, with a gaze-angle dose optimization can be broken down into the following steps. The first step is the acquisition of high-resolution 3D MRI images. Afterwards, a semi-automatic segmentation of all relevant structures is performed for 3D MRI-based patient-specific eye reconstruction, which is used for the next step, calculation and evaluation of the dose distribution within the eye. The last step is a forward optimization to improve and simplify the selection of the optimal gazing angle(s) for the treatment.

2.B. Patients and data collection

Eight patients referred by the Department of Ophthalmology at Leiden University Medical Center were diagnosed in 2018 with a primary uveal melanoma and no evidence of extrascleral extension. All patients were retrospectively included in this study (Fig. 1). Five patients had right and three patients left eye melanomas (Table I). The uveal melanomas involved the equator in 37.5% of the patients and were located posteriorly, meaning at a maximum 3-mm distance[2] of the optic nerve in 67.5% of the cohort. The median tumor thickness and basal diameter were 6 and 12 mm, respectively (ranges: 3 to 12 mm and 8 to 18 mm). Three patients had T1 melanoma, 2 at T2 stage and 3 at T3 stage according to the international Tumor Node Metastasis (TNM) classification.[28] The closest mean border-to-border 3D surface-mesh distance from the tumor to the optic nerve was 2.6 mm (median, min, max) = (1.5, 0, 12 mm) and to the macula was 3.9 mm (median, min, max) = (3.7, 0, 14 mm). MR-tumor prominences and thicknesses were manually measured by the same ocular radio-oncologist and TNM classification followed the consensus staging forms from the American Joint Committee on Cancer, Eighth Edition.[28]

With the aim of providing a comparison between the current geometrical approach and the proposed 3D MRI-based treatment planning approach, additional clinical information was collected for patient 3, who presented a macular area tumor. For this patient, tumor dimensions were determined using high frequency ultrasound images (10MHz, Quantel Medical Aviso, Cournon d'Auvergne, France): prominence = 4 mm; diameter (min × max) = (11.8 × 12.0 mm). Visual inspection of fundus photography was used to adjust
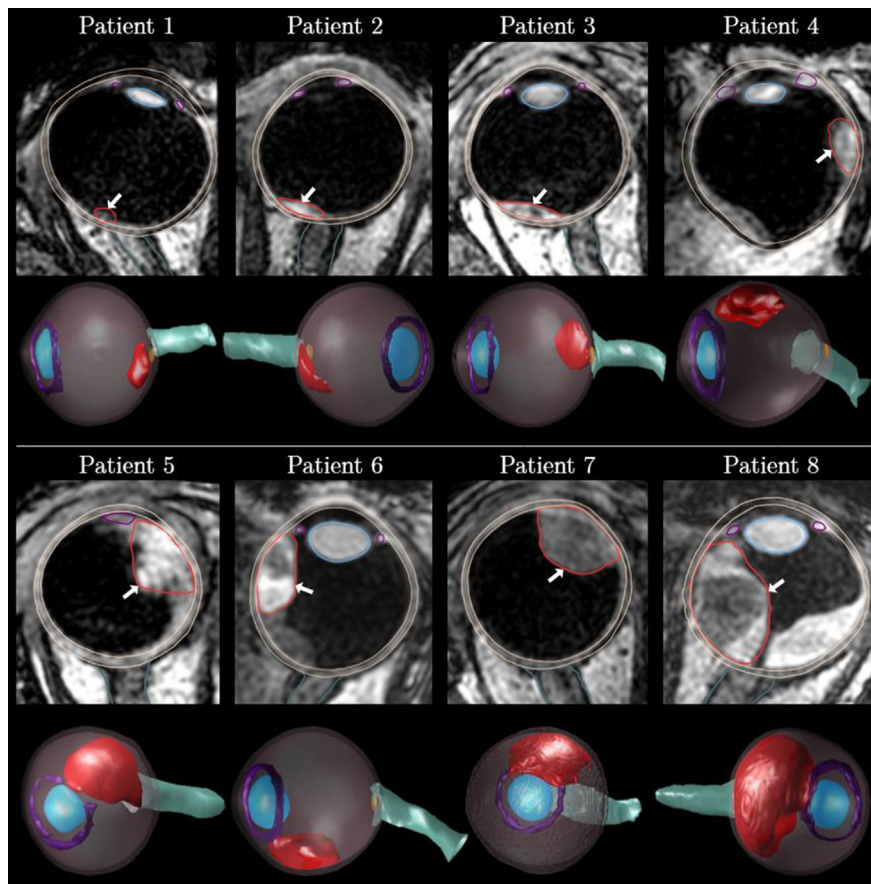
FIG. 1. Patient cohort. Three-dimensional (3D) T1-weighted magnetic resonance (MR)-slices and reconstructed eyes with segmented MR contours: lens (blue); ciliary body (purple); optic nerve (green); sclera ring (beige); tumor (red). The white arrows indicate the uveal melanoma. Note that the macula (orange) is ellipsoidal-like shaped and only visible through the 3D-reconstructed MR-eyes, temporal side to the optic nerve head.

the contour of the tumor base and determine an accurate macula positioning.

2.C. Ocular imaging data

2.C.1. 7 Tesla high-resolution MRI patient imaging protocol

For the development and testing of the high-resolution MRI ocular proton therapy treatment planning approach, MRI data from a single institution were collected. The study was approved by the Institutional ethics board and followed the recommendation of the Declaration of Helsinki. Written informed consent was obtained from all the patients of the study prior to their MRI scan. The orbits were imaged with a Philips 7 Tesla Achieva whole-body MRI (Philips Healthcare, Best, The Netherlands). A dedicated mask supporting a custom-made three-channel micro-eye-coil array has been designed in-house and wore by every patient. The patient head was immobilized in a volume transmit head coil (Nova Medical Inc., Wilmington, MA, USA). None of retro- or peri-bulbar anesthesia was provided during the MRI acquisition; the patients were instructed before the scan to adhere to the cued blinking acquisition scheme. They were asked to alternatively focus on a Maltesian cross, while quickly blinking their eyes at an indicated time of every 3 s. Sequences to offset eye-motion artefacts were performed, as previously described.[22–24] The complete MR-protocol included two scans with an isotropic resolution, specifically designed for radiotherapy planning. Parameters were as follows:

1. Three-dimensional gradient echo T1-weighted scan (TI/TR/TE/FA: 1280 ms/5.4 ms/2.4 ms/7 deg); FOV: 40 mm × 45 mm × 38 mm; isotropic voxel size resolutions: $(0.6 \text{ mm})^3$ for acquisition and $(0.3 \text{ mm})^3$ for reconstruction.
2. Three-dimensional turbo spin echo T2-weighted scan (TR/TE: 2500 ms/203 ms with SPIR); FOV: 40 mm × 47 mm × 38 mm; isotropic voxel size resolutions: $(0.6 \text{ mm})^3$ for acquisition and $(0.3 \text{ mm})^3$ for reconstruction.

These two dedicated clinical MRI protocols enabled to perform imaging in a scan time of 3 min and 3 s for T1-weighted images and 2 min and 53 s for T2-weighted images. Additionally, contrast-enhanced T1-weighted images

TABLE I. Patient cohort tumor characteristics and dosimetric results.

Patient	1	2	3	4	5	6	7	8
Localization[a]	R	L	R	L	R	R	R	L
Tumor lesion site[b]	P	P	P	E	P	E	E	P
MRI tumor prominence — diameter (mm)	4–8	3–9	3–10	5–14	8–10	7–16	9–14	12–18
Closest distance to ON[c] — to M[d] (mm)	1–0	1–2	0–0	10–6	2–5	7–9	12–14	0–3
AJCC TNM staging[e]	T1	T1	T1	T2	T2	T3	T3	T3
Dosimetric results[f]								
$V_{95\%}$ tumor coverage (%)	99.90	99.53	100.00	99.11	98.41	98.69	97.48	98.47
D_{max} optic nerve (%)	16.53 (10.95–69.27)	88.05 (47.24–100.00)	58.50 (27.08–98.33)	6.98 (0.00–71.49)	23.94 (0.00–68.95)	32.50 (0.00–94.22)	10.90 (0.00–36.40)	92.86 (62.04–100.00)
D_{mean} lens (%)	30.19 (0.00–69.91)	45.70 (0.00–83.99)	56.51 (0.00–73.35)	2.62 (0.00–92.85)	55.14 (41.66–93.33)	28.70 (18.52–91.60)	64.22 (55.28–91.80)	88.82 (53.87–93.73)
D_{mean} ciliary body (%)	27.36 (0.00–65.33)	38.36 (0.00–78.02)	40.54 (0.00–68.36)	21.33 (0.12–86.56)	42.27 (33.91–92.08)	29.41 (18.97–87.26)	49.03 (41.21–87.76)	75.32 (46.76–92.57)
D_{mean} sclera ring (%)	30.76 (20.15–34.39)	38.81 (18.10–56.27)	44.69 (26.95–49.59)	27.45 (23.15–44.36)	39.08 (35.35–53.03)	32.69 (28.45–42.79)	39.89 (32.62–48.56)	64.25 (60.00–75.40)
D_{max} macula (%)	100.00 (100.00–100.00)	100.00 (88.46–100.00)	100.00 (100.00–100.00)	0.00 (0.00–100.00)	94.74 (0.00–100.00.00)	13.64 (0.00–100.00)	0.00 (0.00–100.00)	100.00 (100.00–100.00)
Objective function values, straight gazing angle[g]								
Iso-weighted	0.92	0.71	0.88	0.46	0.68	0.64	0.62	0.78
Optic nerve prioritized	0.98	0.94	0.99	0.90	0.94	0.94	0.90	0.96
Macula prioritized	0.98	0.94	0.97	0.08	0.40	0.54	0.13	0.96

[a]**Localization:** R: Right eye; L: Left eye.
[b]**Tumor lesion site:** (E) At equator; (P) Posterior pole.
[c]**ON:** Optic nerve.
[d]**M:** Macula.
[e]**AJCC TNM Staging:** Uveal melanoma staging from American Joint Committee on Cancer[28] .
[f]**Dosimetric results:** Mean tumor coverage achieved for the set of gazing angles. Average dosimetric results over the solutions space of every patient for D_{max} to the optic nerve and to the macula, and D_{mean} to the lens, the ciliary body and the sclera ring. Results presented by D_{median} (D_{min} - D_{max}) relative proton absorbed dose in the considered ocular organ (%).
[g]**Forward optimization with OPT'im-Eye-Tool.** Value of the global weighted-sum objective function obtained for the straight gazing angle for three different prioritizations: iso-weighted, optic nerve prioritized and macula prioritized.

were acquired after intravenous injection of 0.1 mmol/kg gadoterate meglumine (gd-DOTA, DOTAREM, Guerbet, Roissy CdG Cedex, France).

2.C.2. Semi-automatic MRI-segmentation

In-house algorithms have been developed to semi-automatically segment eye anatomies and uveal melanomas on no contrast-enhanced T1- and T2-weighted images.[29] The center of the eye was estimated on T2-weighted images using the fast-radial symmetry transform.[30] This center was used to build a 3D-triangulated-surface mesh to detect the inner and outer borders of the sclera and the tumor boundary itself. The inner scleral mask (including the cornea) was created to register T1- and T2-weighted images using Elastix,[31,32] with normalized mutual information as a similarity metric. Vitreous body and lens segmentations were carried out on axial T1-weighted images using fuzzy C-means clustering. These masks were subsequently subtracted from the sclera mask to segment the tumor. Once the tumor segmentation step was completed, the contrast-enhanced T1-weighted images were used to assess and manually validate that no retinal detachment was actually included within the tumor volume. Knowing that the ciliary body expands the lens structure, its segmentation was performed as follows: the two perpendicular axis maximizing the geometry of the lens in the axial plane where found by applying principal component analysis. The shortest axis of the lens (anterior–posterior direction) was used to locate two perpendicular planes located in the upper and lower extremes of the lens structure. The volume constrained by these planes along the consecutives MRI slices established the searching space where the ciliary body had to be contained. By using an iterative closest point algorithm, an inscribed polygon superquadric (i.e., donut-like shape), and centered at the center-of-mass of the lens, was fitted to the boundaries of the ciliary body. In the current implementation, the ring-shaped ciliary body segmentation consists mainly of the ciliary muscle. The parts of the ciliary body anteriorly attached to the sclera as well as the suspensory ligaments connected to the lens are hardly differentiable on our MRI images with the dedicated protocols developed for radiotherapy planning purposes. The optic nerve sheath was segmented on T1-weighted image using tubular tracking algorithm, after defining a seed point on the optic nerve, followed by mesh fitting. The algorithms were developed using the rapid-prototyping platform MeVisLab (Fraunhofer MeVis, Bremen, Germany). The macula was determined as an ellipsoid and its position was based on a geometrical definition[33] as it is not visible on MRI. It followed the geometrical approximation currently implemented in the TPS Eclipse Ocular Proton Planning (EOPP, Varian Medical Systems, Inc., Palo Alto)[33], that is, a longitudinal radius of 1 mm, a transversal radius of 0.44 mm and a thickness of 1.5 mm. The skin plane was defined as a plane parallel to the surface entrance and passing through the center-of-mass of the 3D-MRI triangulated-surface mesh of the lens. However, both macula position and skin plane distance from the anterior

cornea can be adjusted to the physical value and position of the individual patient. As retractors will be used during the treatment to keep eyelids away from the beam path, the eyelids were not delineated as OARs.

2.C.3. Ocular motility

To complete the solutions space with all the gazing angles, a 3D rotational movement of the eye was simulated. The eye orientation was described by a sequence of rotations using the modified IEC 61217 fixed horizontal beamline notation convention. The primary position of the eye was defined as the rest position, corresponding to a straight gazing angle. All other positions were defined according to the gazing direction. The center of rotation was defined as the center-of-mass of the 3D-MRI triangulated-surface mesh of the sclera ring[29] (see supplementary materials) and its position was considered the same for all the gazing angles over the solutions space.

2.D. πDose and beam shaping patient-specific components

An in-house developed dose engine πDose (Proton Eye Dose) has been used for this study. πDose is based on a semi-analytical broad beam algorithm similarly to the one proposed by Koch and Newhauser.[34] The supplementary materials section provides details about the algorithm and its preliminary validation.

Essential beam modifying devices that are always present during the irradiation, that is, including scatter foils, variable range shifters, range modulator wheels and beam collimator, have been implemented. The first three beam modifying devices are beamline-dependent and their physical properties are defined during the commissioning and summarized in look up tables for computational efficiency. Variable range shifters and range modulator wheels are used to improve the dose distribution conformity in depth, as a single native Bragg peak is insufficient to shape the dose to cover the target volume. A spread-out Bragg Peak (SOBP) was created by adding contributions of individual weighted Bragg peaks generated by the range modulator wheels. The plateau of the SOBP was normalized at 100% of the maximum dose. The definitions of the depth of the penetration (i.e., the range R_{90}) and the width of the SOBP were characterized by the International Commission on Radiation Units and Measurements, report 78.[35] The width of the SOBP was defined by the length of the tumor with addition of 2.5-mm margin distally and proximally in the gazing direction and along the beam central axis. Currently, the dose calculation is relative but it might be translated to absolute dose for a fully characterized beamline.

The beam collimator is patient-specific and shapes the dose laterally based on the Beam's-Eye-View of the tumor contour with an added circumferential lateral margin back projected at the snout location. The lateral margin was 2.5-mm expansion of the Gross Tumor Volume. For treatment

planning purposes, the collimator was assumed to be an ideal absorber, acting as an infinitesimal thin and completely absorbent material, while the proton beam was also assumed to be uniform. All the plans were created with the 50% isodose encompassing the target with the margin laterally.

All the three margins (lateral, distal and proximal) were defined based on a worldwide clinical consensus.[8,9,15,17,36–39]

2.F. OPT'im-Eye-Tool: a forward gazing plan quality optimization

An interactive manual decision-making tool has been developed for the gazing angle optimization. The tool was based on global weighted-sum objective functions computed for each gazing angle. Those functions were calculated for all ocular structures to be spared during the treatment. Each structure can be prioritized by modifying weights to a specific dose-volume parameter, for example, the mean dose (D_{mean}) to the lens, the ciliary body and the sclera, and maximum dose (D_{max}) to the optic nerve and the macula. Additionally, a linearly defined parameter was used to penalize extreme gazing angles located at the periphery of the patient's field of view. For example, zero penalty was given for the primary position (straight gaze) where the extraocular muscles exhibit minimum force so it is the easiest gazing angle to hold for a patient, whereas extreme gazing angles at the periphery of the field of view received the highest penalties. The tumor coverage was not included in the optimizer, as the definition of the broad beam ensures full coverage of the target volume.

The forward optimization process was performed by calculating the dose distribution for all the gazing angles of the solutions space. Objective function values were retrieved. Planners can change OAR weights on a trial-and-error basis to evaluate how prioritization affects the optimal gazing angle selection. Weights were strictly positively defined and summed up consistently to unity. A gazing angle-dependent map has been developed to visualize the global weighted-sum objective function values, where each calculated gazing angle function value was displayed by the two angles [Ψ; ϕ]. Ψ represents any elevation/depression of the eye, whereas ϕ represents any ab-/adduction (Fig. 3). For this study, parameters Ψ and ϕ defined the patient field of view and ranged between -30 to $+30$ degrees with an increment of 3 degrees for both elevation/depression and add-/abduction. This mapping mimics the in-room gazing template which will be used to guide the patient gazing direction using an LED light. The optimal gazing angles ranges can be selected by the lowest global weighted-sum objective function values.

3. RESULTS

3.A. Dose distributions over the gazing angles solutions space

An example of 3D T1- and T2-weighted MR-slices with delineation and the relative proton dose distribution

calculated with πDose is shown for patient 6 (Fig. 2). Table I summarizes the dosimetric results for the whole cohort. The resulting ipsilateral doses to OARs, D_{max} to both optic nerve and macula and D_{mean} to the lens, ciliary body and the sclera ring are also detailed in Table I. For all 441 simulated gazing angles per patient, the target coverage including margins ($V_{95\%} > 95\%$) was always achieved. The table presents the average of all dosimetric results over the gazing angles solutions space for every patient, presented by D_{min}, D_{median} and D_{max} relative proton absorbed dose in the considered ocular volume of interest (%).

Examples of interactive planning obtained from the OPT'im-Eye-Tool optimizer are shown in Fig. 3, which display the gazing angle-dependent grid maps. In an iso-weighted situation, the weights for the five OARs and for the gazing angle were equally set to 0.17 whereas in either the optic nerve or macula prioritized situations, weights were assigned to 0.8 for the optic nerve (or macula) and 0.04 to other OARs. Each colored area represented a specific gazing angle, conjugated by a coupling of [Ψ_i; ϕ_j]. The values of the function obtained for the straight gazing angle for the patients of the cohort and for all three prioritizations are also given in Table I. For posterior T1 tumors near the optic nerve and macula (patients 1 to 3), only well-defined extreme gazing angles located at the periphery of the field of view would result in acceptable global weighted-sum objective function values; otherwise, any change on gazing direction would result in high global weighted-sum objective function values in both optic nerve and macula prioritizations. Equatorial tumors (i.e. patients 4, 6, 7), due to their localization and distance further away from critical OARs, enable more choices to select optimal gazing angles, especially in the attempt of sparing the macula. Regarding patient 4, the values of the objective function for the straight gazing angle were 0.46 (iso-weighted prioritization), 0.90 (optic nerve prioritization) and 0.08 (macula prioritization). To this end, looking straight or downward would be more suitable for macula sparing in that patient. For patient 6, who had a T3 equatorial tumor, the distance between the tumor and both optic nerve and macula edges were 7 and 9 mm, respectively, which enables a full sparing of these two ocular organs. Although, an attempt to spare the optic nerve would result in selecting one gazing angle located at the periphery of the field of view, looking straight would be suitable for a full sparing of the macula. For patient 5, who had a posterior T2 tumor, gazing at the straight direction would be optimal for macula sparing (objective function value of 0.40, Table I); on the other hand, if the highest priority would be given to spare the optic nerve, the straight direction should be avoided (objective function value of 0.94, Table I). Patient 8 had a T3 nasal tumor almost fully covering the optic nerve and its tumor edge was located more than 3 mm away from the macula. In this situation, top quadrant of the gazing mapping corresponding to eyeball elevation would be the optimal solution in an iso-weighted situation; optic nerve and macula situations resulted in high function values for the straight gazing angle (0.96 both), which should be avoided.
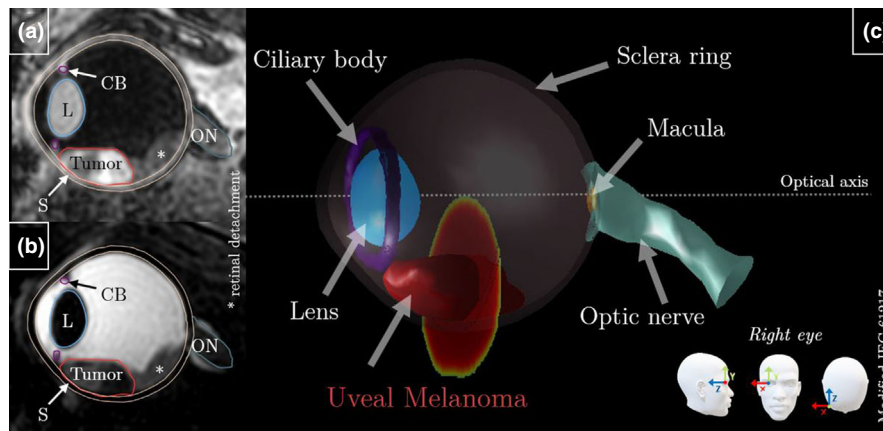
FIG. 2. Demonstration of developed planning tools: three-dimensional (3D) T1- (a) and T2-weigthed (b) magnetic resonance (MR)-slice showing the uveal melanoma and delineated MR ocular anatomical structures (ON: Optic nerve; L: Lens; CB: Ciliary body; S: Sclera ring. (c) 3D relative proton dose distribution within the 3D-MR-based reconstructed eye, calculated by πDose. The macula is geometrically defined.
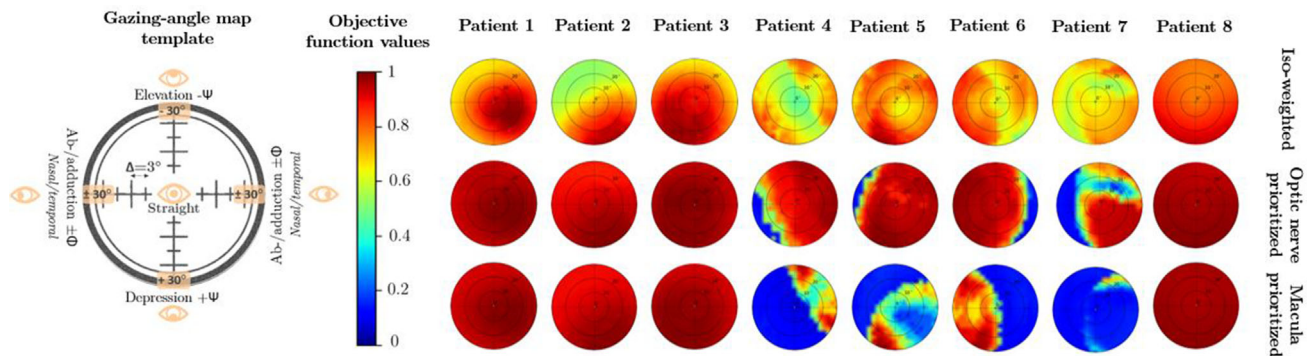

FIG. 3. Resulting gazing-angle dependent heat maps depicting the global weighted-sum objective function values in iso-weighted, optic nerve prioritized and macula prioritized optimizations. The colder colors (in blue) represent the lower objective function values, and therefore, preferable gazing angles for a treatment. Field of view ranged between −30 to +30 degrees, both for add-/abduction and elevation/depression, with increments every 3 degrees. A total of 441 gazing angles were simulated for every patient.

3.B. Comparison with geometrically based treatment planning concept

To demonstrate the geometrical and dosimetrical accuracy of the developed treatment planning system, a treatment plan for patient 3 with a small T1 posterior tumor was created in EOPP as well as in πDose (Fig. 4). Fundus photography and ultrasound images were used to generate a geometrical model of the eye and target structure in EOPP as well as to check the outcome of the MR-tumor base delineation and macula positioning. A straight gazing angle was chosen in both planning systems to provide a clear demonstration of the similarities and differences between the two approaches. Both systems resulted in the same range penetration and range modulation within 1 mm agreement. The shapes and volumes of the target and OARs are different.

4. DISCUSSION

In this study, the feasibility of implementing a high-resolution 3D MRI-based treatment planning approach with a gaze-angle proton dose optimization into one platform dedicated to the treatment of ocular tumors has been presented. MR-based reconstruction of the patient eye without any surgical clip was performed with a semi-automatic segmentation of the ocular structures and tumor. The segmentation was incorporated into an in-house developed treatment planning system based on a semi-analytical broad beam algorithm. The dose calculation with a forward gazing angle optimization was then performed directly on the reconstructed MR-eye.

The first particularity of the modern treatment planning system for ocular proton therapy proposed in the study, is the use of 3D MRI to segment the eye and the relevant structures of an individual patient eye anatomy. This approach can reduce the discrepancies and uncertainties in volume and shape definition that exist within the generic geometrical models currently used in clinics, which are not patient-specific.[40–42] Along the manuscript, it has been demonstrated (Fig. 4) that our in-house developed treatment planning system is geometrically and dosimetrically accurate. However, all delineated structures differ in shape and size in comparison to the clinically used geometrical approach, due to the
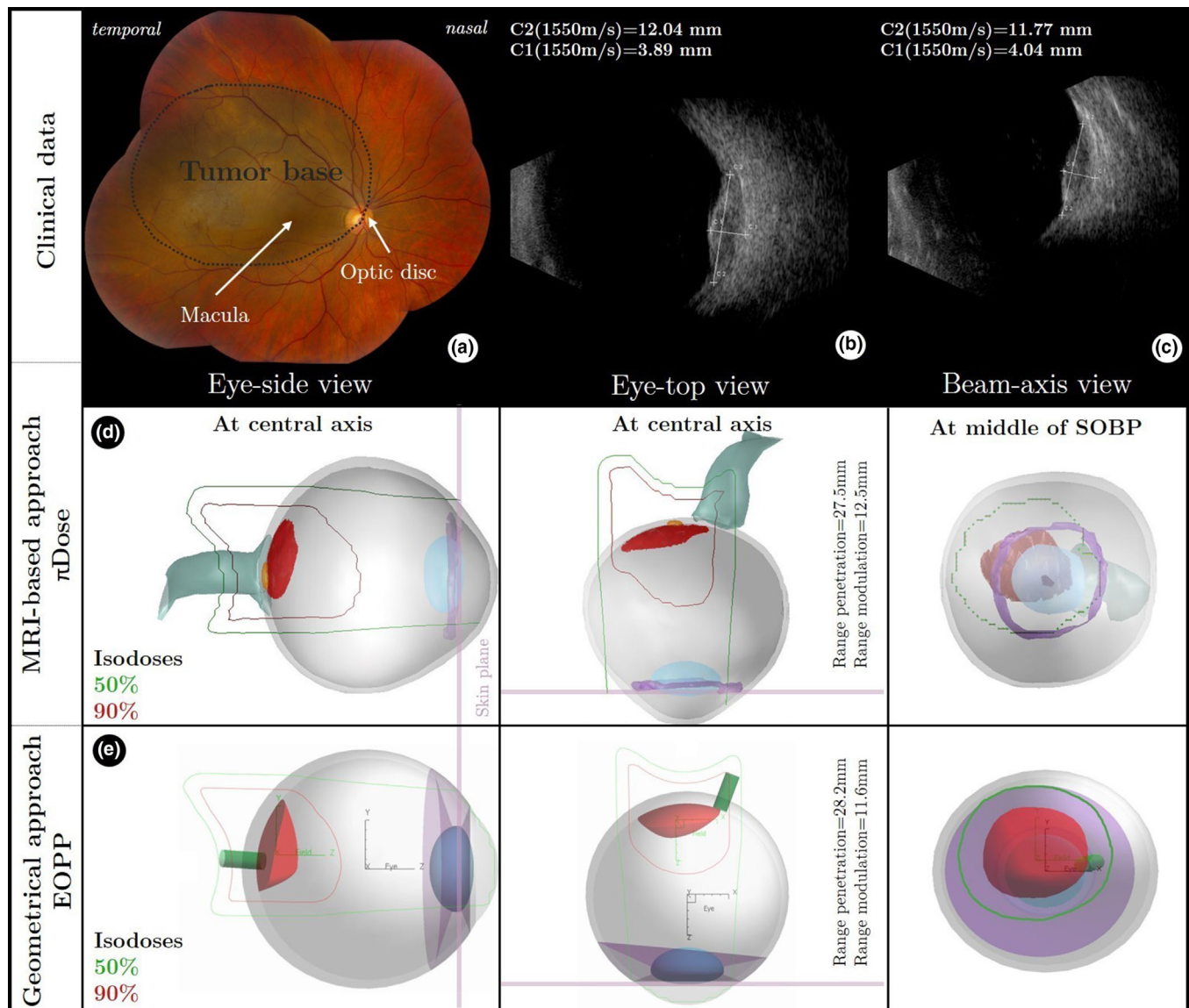
FIG. 4. Treatment plan comparison for patient 3 (T1 posterior tumor). (a) Fundus photography and (b, c) Ultrasound images. (d) Three-dimensional magnetic resonance imaging (MRI)-based reconstructed eye and πDose treatment plan. The macula (orange) is geometrically shaped. Fundus photography was used in conjunction with MR information for macula positioning and appreciation of the tumor base delineation. (e) Geometrical approach and EOPP TPS treatment plan. Eye and tumor were modeled based on the ultrasound images and fundus photography.

intrinsic differences between both methods, which hampers a proper comparison between our output vs the current clinical practice. Therefore, intensive investigation involving larger cohort of patients are required to carefully adapt the current clinical concepts to MRI-based treatment planning, in order to exploit its full potential and to maintain high local tumor control. New definition of margins as well as organs-at-risk constraints is likely to be needed. Rigorous quantification and mitigation of treatment-related uncertainties should be part of these studies.

Despite the availability of advanced sophisticated ocular biomechanical models as well as recent methods such as Statistical Shape Models,[27,43] simple geometrical modeling based on ellipsoidal eye shape remains the current standard deployed into the TPS such as EYEPLAN[44–46] and Eclipse

Ocular Proton Planning (EOPP, Varian Medical Systems, Inc., Palo Alto).[33] The geometrical models are scaled close to the individual anatomy using patient-specific parameters such as naso-temporal, sagittal, anteroposterior and limbus diameters of the eye as well as the edge of the tumor to papilla distance and interclips distances. These dimensions and measurements are based on intraoperative caliper measurements and information from fundus photography,[46] ocular biometry, ultrasound images and/or CT/MRI. Nevertheless, those geometrical models may in some cases significantly differ from the real patient anatomy. Slopsema et al.[18] recently evaluated the differences in clip position between an eye definition based on geometrical modeling as provided by the EYEPLAN TPS and a modified eye model based on CT-guided simulation. They demonstrated that the position of the

clips is more accurately modeled for specific cases in the latter when 3D CT information was incorporated.

Hitherto, only the OCTOPUS TPS enables fine scaling of the eye model dimensions according to CT or MRI data. However, none of the ocular structures can be segmented directly from the MRI. Their definitions are still based on the model itself. EYEPLAN as well as EOPP TPS define the target by modeling the shape of the tumor by using appropriate degrees of a polynomial function that would match the best the complexity of the uveal melanoma. Marnitz et al.[47] compared clinical tumor volumes generated by both EYEPLAN and OCTOPUS, which derived from T1w and T2w 1.5 T MRI slices with a dedicated surface coil. They observed a systematic reduction of the clinical tumor volumes in the OCTOPUS TPS over their patient cohort by a mean factor of 2.3 (T2w-based) and 1.7 (T1w-based), meaning that a model-based method always overestimated tumor volumes. For an accurate 3D description of the tumor and organs-at-risk, it is crucial that 3D isotropic sequences are performed, since multi-slice sequences suffer from through plane motion artefacts as not all slices are acquired simultaneously. This through plane motion results in significant deformation of the image in the slice direction, preventing an accurately reconstructed MR-eye.

Although earlier studies have already reported on the use of MRI for the diagnosis and, to a lesser extent, for the treatment planning of uveal melanomas purpose,[40,48,49] the clinical impact of these studies was somewhat limited due to the relatively low resolution images compared to current state-of-the-art of MRI protocols in ocular oncology.[23,24,26,50] In this study, the increased signal at 7 Tesla MRI was employed, but the recent advances in clinical 3 Tesla MRI allow for scans with a similar 3D resolution. In order to achieve the same image quality with a 3 Tesla MRI as with a 7 Tesla MRI, our recent efforts have focused on developing digital receive chains. A single coil is usually used to receive the 3 Tesla MRI signal, but the integration of multi-element receive coils would allow a significant reduction of the scanning time.[23] The proposed 3D MRI-based treatment planning is field-strength independent, thus enabling for a swift transition to clinical practice.

A $(0.3 \text{ mm})^3$ voxel size defining the 3D isotropic resolution of the reconstructed MRI images was used for the semi auto-segmentation of optical structures and tumor volume. This resolution is about twice as high as the inter observer variability occurring with ultrasound measurements,[51] which is still the gold standard to determine base and maximum tumor prominence. Nowadays, 3D MR-images with such a resolution are sufficient to precisely and consistently assess a wide spectrum of tumor dimensions, even regarding very small tumors.[24] Another relevant clinical concern relates to an unclear presence of a flat extension.[52] Although with MRI, very small uveal melanoma can be visualized,[24] flat extensions of the tumor, which are less than a millimeter thick, can easily be missed. The reconstructed patient MR-eye should therefore always be validated with the fundus photography and any other available biometry measurements,

which were acquired for the diagnosis and therapy selection. Even in the fully automated MRI-based treatment planning workflow, the use of a multimodal imaging for diagnosis and patients follow-up purposes remains indubitably important.[52] The recent advances in anatomical and functional ophthalmic MRI have spotted key parameters[24] when imaging uveal melanomas with good quality images, resulting in substantial help in tumor contouring-making process. For some patients (e.g., Fig. 1, patient 8) though, subretinal hemorrhage occurring near the uveal melanoma may raise discussions while evaluating the tumor edge. In these specific cases, the final decision should therefore be achieved within a multi-disciplinary consensus.

Regarding the delineation of the organs-at-risk, the main limitation was to segment the macula which was not visible on any of the tested MRI sequences and therefore, only geometrical assessment of its position and shape was implemented. The difference in the optic nerve segmentation between EOPP TPS and the MRI-based approach has multiple reasons. The optic nerve in EOPP TPS is of tube-like shape, and invariant during eye rotation. The tube has a limited length and the optic disc diameter has a fixed value that cannot be modified by the user. It is the main important limitation as the optic nerve shape is highly patient-dependent. The ciliary body delineation is different to the geometrical approach as only ciliary muscle is differentiable on the developed MRI sequences. Improvement of ciliary body delineation as well as assessment on MR of macula and lacrimal gland delineation (preventing dry eye syndromes[53]) is subject of further studies.

None of the currently available treatment planning systems directly incorporates 3D data for calculating the dose distribution within the ocular structures. Dose calculation in the EYEPLAN and EOPP TPS works with a surface sampling (nodes) for isodoses generation. In the OCTOPUS TPS, the real-time dose calculation is performed on the surface of the eye model by modeling isodose surfaces as cylindrical layers from the tessellated uveal melanoma boundaries including safety margins.[54] This is not directly performed in 3D voxels, leading to a loss of information for very small ocular structures, which cannot be recovered.[20,55] Dose calculation engine πDose was developed in this study enabling the dose calculation in 3D. However, it should be stressed that the dose calculation remains crude, accounting in a tabulated fashion for generic beam modifying devices. Therefore, further work still has to be performed during the commissioning phase to tune the algorithm specifically to a specific beamline such as the one available at HollandPTC (Delft, The Netherlands), and to include the physics and dosimetric characteristics of each beam modifying device.

In daily clinical practice, the choice of the optimal gazing angle has to allow acceptable sparing of the most relevant ocular organs-at-risk. In both available TPS, EYEPLAN and EOPP, the selection of the optimal gazing angle is performed by manual rotation of the eye model and evaluation of the dose distribution. A complementary approach was recently introduced by Hennings et al.[19] with the concept of gazing

angle-dependent mapping, where the number of organs-at-risk with violated dose-volume constraints was displayed. In their work, a tool for semi-automatic dose evaluation of all clinically achievable gazing angles was built and the validity of this concept was tested in a cohort of 48 patients. Conversely, in the approach presented in this manuscript, the proton dose distribution was calculated for every achievable gazing angle and displayed as a grid map of values for the global weighted-sum objective function. A trade-off for organs-at-risk was manually and interactively obtained during a forward optimization over the gazing angles of the solutions space and tailored to the patient at hand, depending on wished-objectives outcomes. This trade-off included a penalty function for extreme gazing angles, which was so far *per se* simple. Additional features will be added into πDose. Firstly, dose optimization using a physical wedge will be investigated, especially to reduce the dose to critical ocular organs or to modify the needed modulation. Secondly, constraints and penalties for the head tilt and the chair position will be included into a sophisticated function as, for example, the tilting the head back makes it easier for a patient to look up, but more difficult to look down. In this work, the calculation of the global weighted-sum objective functions still remains a manual and time-consuming process but it is a first step towards a more complex optimization in ocular proton therapy, including above-mentioned features. A user-friendly interface was developed to guide this planning step. Therefore, by bringing everything together, another step might be an automated multi-criteria optimization integrated into the pipeline of πDose.[56] This step will influence the complexity of the algorithm but will not affect the speed of the calculation over the whole solutions space by automatically selecting the optimal gazing angle(s) configuration.

During the treatment planning, commonly 2.5-mm margins are used. These margins encompass the following[57]: (a) uncertainties in the physics setup beam line (including stopping power ratio, range, penumbra); (b) uncertainties in the axial eye-length and tumor height measurements via A- and B-scans ultrasonography and ocular biometry; (c) uncertainties in the geometrical eye model including clip positioning error; (d) uncertainties in patient eye positioning and rotation; and (e) inaccuracy in the in-room alignment with X-ray images. The first and last aspects might only be improved by technical developments coming up the next decades, which in turn could increase accuracy of commissioning. However, considering the dosimetric properties of the eyelines worldwide using a passive scattering system, it is unlikely that substantial improvement will emerge from this area. With regards to points (b) and (c), a dedicated 3D MRI-based treatment planning approach will help to mitigate uncertainties at the level of treatment planning, as the uveal melanoma, eye globe and ocular structures can be more accurately segmented. With regard to the patient eye positioning and rotation, eye ball translation and involuntary eye movements motion models, which are so far neglected in ocular proton therapy planning, could be introduced and eventually, it could mitigate these uncertainties. As in conventional radiotherapy,

limitation of these uncertainties, together with consideration of random and systematic errors during the whole treatment process, might lead to a better definition of margins in ocular proton therapy. In fact, elaborating such a theoretical margin recipe instead of using the consensus of 2.5-mm margin can lead to a better organs-at-risk sparing. This recipe can result in reduced complication probability while keeping the same local tumor control for some clinical situations.

An ultimate aim of using MRI in ocular proton therapy is a clipless treatment and to increase patient comfort. To achieve this, not only an MRI-based TPS is needed but also a real time eye detection system for gazing angle position verification before and during the treatment.[58] At both Centro Nazionale di Adroterapia Oncologica (CNAO, Pavia, Italy) and Paul Scherrer Institute, eye tracking systems have been embedded for controlling the gaze direction during the treatment fraction.[59–62] An infrared optical tracking-based camera system is also under development within a broader collaboration of this project for Image Guidance Proton Therapy (IGPT). The clinical implementation of any of the investigated systems will lead to avoiding the use of surgical clips (tantalum, 2.5-mm diameter, 0.17-mm thickness), which cause dose uncertainties behind and/or nearby due to the high density of tantalum if located in the beam path. The density of the tantalum material is not taken into account in both EYEPLAN and EOPP TPS where only an average of eye density of 1.05 g.cm^{-3} is assumed, although this value may be adjusted and vary among the centers.[13,63] The degree of disturbance can be high as raised by Carnicer et al.[64] who established an underdose shadow of up to 20% downstream of their location associated with an overdose on either side of the beam paths and a shift reduction of 1.1 mm of the intended range along the central axis of the beam. Newhauser et al.[65] reported dose perturbations between 22% and 82%, when investigating various clip positions and orientations. Likewise, the presence of acute hemorrhage or severe cataract for some patients may disturb the clips placements, which, in turn, may entail lower accuracy of tumor delineation.[63] Egger et al.[5] highlighted the fact that inadequate positioning of tantalum clips has compromised tumor modeling and thus is identified as a risk factor for local tumor control failure if the target definition would be based purely on the X-ray imaging. Although attempts have been studied for substituting tantalum with other fiducial markers materials,[66,67] tantalum still remains the implanted metal of choice. Last but not least, the stitching of the clips to the sclera is an invasive procedure significantly reducing the patient comfort during the treatment. Therefore, by avoiding clips in a well-established way, a 3D MRI-based treatment planning approach using an automatic gaze-angle optimization linked with a dedicated eye tracker for daily treatment setup control could be the key to advance ocular proton therapy.

5. CONCLUSION

In conclusion, accounting for real 3D ocular anatomy is feasible using high-resolution MRI, and a dedicated

treatment planning system has been successfully developed. This new combined approach could lead to better selection of the gazing angles depending on weights and organs-at-risk constraints. This represents an important step towards a non-invasive clinical protocol and improved treatment accuracy. It opens additional investigation possibilities for ocular papilla and macula MR segmentation, margins definition, multi-criteria optimization, workflow validation, and clipless IGPT procedure, which are the scope of ongoing and further research.

ACKNOWLEDGMENTS

CONFLICT OF INTEREST

[a)]Author to whom correspondence should be addressed. Electronic mail: e.fleury@erasmusmc.nl.

REFERENCES

1. Gragoudas ES, Seddon JM, Egan K, et al. Long-term results of proton beam irradiated uveal melanomas. *Ophthalmology*. 1987;94:349–353.
2. Courdi A, Caujolle JP, Grange JD, et al. Results of proton therapy of uveal melanomas treated in Nice. *Int J Radiat Oncol Biol Phys*. 1999;45:5–11. http://www.ncbi.nlm.nih.gov/pubmed/10477000. Accessed June 25, 2019.
3. Hrbacek J, Mishra KK, Kacperek A, et al. Practice patterns analysis of ocular proton therapy centers: the international OPTIC survey. *Int J Radiat Oncol Biol Phys*. 2016;95:336–343.
4. Thariat J, Rahmi A, Salleron J, et al. Proton beam therapy for iris melanomas in 107 patients. *Ophthalmology*. 2018;125:606–614.
5. Egger E, Schalenbourg A, Zografos L, et al. Maximizing local tumor control and survival after proton beam radiotherapy of uveal melanoma. *Int J Radiat Oncol Biol Phys*. 2001;51:138–147.
6. Fuss M, Loredo LN, Blacharski PA, Grove RI, Slater JD. Proton radiation therapy for medium and large choroidal melanoma: preservation of the eye and its functionality. *Int J Radiat Oncol Biol Phys*. 2001;49:1053–1059.

7. Höcht S, Bechrakis NE, Nausner M, et al. Proton therapy of uveal melanomas in Berlin: 5 Years of experience at the Hahn-Meitner Institute. *Strahlentherapie und Onkol*. 2004;180:419–424.
8. Damato B, Kacperek A, Chopra M, Campbell IR, Errington RD. Proton beam radiotherapy of choroidal melanoma: the Liverpool-Clatterbridge experience. *Int J Radiat Oncol Biol Phys*. 2005;62:1405–1411.
9. Dendale R, Lumbroso-Le Rouic L, Noel G, et al. Proton beam radiotherapy for uveal melanoma: results of Curie Institut-Orsay proton therapy center (ICPO). *Int J Radiat Oncol Biol Phys*. 2006;65:780–787.
10. Caujolle JP, Mammar H, Chamorey E, Pinon F, Herault J, Gastaud P. Proton beam radiotherapy for uveal melanomas at nice teaching hospital: 16 years' experience. *Int J Radiat Oncol Biol Phys*. 2010;78:98–103.
11. Verma V, Mehta MP. Clinical outcomes of proton radiotherapy for uveal melanoma. *Clin Oncol*. 2016;28:e17–e27.
12. Weber B, Paton K, Ma R, Pickles T. Outcomes of proton beam radiotherapy for large non-peripapillary choroidal and ciliary body melanoma at TRIUMF and the BC cancer agency. *Ocul Oncol Pathol*. 2016;2:29–35.
13. Kacperek A. Ocular Proton Therapy Centers; 2012:149–177. https://doi.org/10.1007/978-3-642-21414-1_10
14. Cirrone G, Cuttone G, Lojacono P, et al. A 62-MeV proton beam for the treatment of ocular melanoma at Laboratori Nazionali del Sud-INFN. *IEEE Trans Nucl Sci*. 2004;51:860–865.
15. Kacperek A. Protontherapy of eye tumours in the UK: a review of treatment at Clatterbridge. *Appl Radiat Isot*. 2009;67:378–386.
16. Afshar AR, Stewart JM, Kao AA, Mishra KK, Daftari IK, Damato BE. Proton beam radiotherapy for uveal melanoma. *Expert Rev Ophthalmol*. 2015;10:577–585.
17. Mishra KK, Daftari IK. Proton therapy for the management of uveal melanoma and other ocular tumors. *Chinese Clin Oncol*. 2016;5:50.
18. Slopsema Rl, Mamalui M, Bolling J, Flampouri S, Yeung D, Li Z, Rutenberg MS, Dagan R. Can CT imaging improve targeting accuracy in clip-based proton therapy of ocular melanoma? *Phys Med Biol*. 2019;64:035010.
19. Hennings F, Lomax A, Pica A, Weber DC, Hrbacek J. Automated treatment planning system for uveal melanomas treated with proton therapy: a proof-of-concept analysis. *Int J Radiat Oncol Biol Phys*. 2018;101:724–731.
20. Pfeiffer K, Dobler B, Rethfeldt C, Schlegel W, Bendl R. OCTOPUS, a planning tool for proton therapy of eye tumours. In: *The Use of Computers in Radiation Therapy*. Berlin, Heidelberg: Springer; 2000:329–331. https://doi.org/10.1007/978-3-642-59758-9_124
21. Dobler B, Bendl R. Precise modelling of the eye for proton therapy of intra-ocular tumours. *Phys Med Biol*. 2002;47:593–613.
22. Beenakker JWM, van Rijn GA, Luyten GPM, Webb AG. High-resolution MRI of uveal melanoma using a microcoil phased array at 7 T. *NMR Biomed*. 2013;26:1864–1869.
23. Beenakker J-W, Ferreira TA, Soemarwoto KP, et al. Clinical evaluation of ultra-high-field MRI for three-dimensional visualisation of tumour size in uveal melanoma patients, with direct relevance to treatment planning. *Magn Reson Mater Physics, Biol Med*. 2016;29:571–577.
24. Ferreira TA, Fonk LG, Jaarsma-Coes MG, van Haren GGR, Marinkovic M, Beenakker JWM. MRI of uveal melanoma. *Cancers (Basel)*. 2019;11:1–20.
25. Oberacker E, Paul K, Huelnhagen T, et al. Magnetic resonance safety and compatibility of tantalum markers used in proton beam therapy for intraocular tumors: a 7.0 Tesla study. *Magn Reson Med*. 2017;78:1533–1546.
26. Graessl A, Muhle M, Schwerter M, et al. Ophthalmic magnetic resonance imaging at 7 T using a 6-channel transceiver radiofrequency coil array in healthy subjects and patients with intraocular masses. *Invest Radiol*. 2014;49:260–270.
27. Nguyen H-G, Sznitman R, Maeder P, et al. Personalized anatomic eye model from T1-weighted volume interpolated gradient echo magnetic resonance imaging of patients with uveal melanoma. *Int J Radiat Oncol Biol Phys*. 2018;102:813–820.
28. American Joint Committee on Cancer. Implementation of AJCC 8th Edition Cancer Staging System. Chicago, IL. https://cancerstaging.org/references-tools/Pages/Cancer-Staging-Resources.aspx. Accessed October, 2020. AJCC; 2017.

29. Beenakker JWM, Shamonin DP, Webb AG, Luyten GPM, Stoel BC. Automated retinal topographic maps measured with magnetic resonance imaging. *Investig Ophthalmol Vis Sci.* 2015;56:1033–1039.

30. De Zanet SI, Ciller C, Rudolph T, et al. Landmark detection for fusion of fundus and MRI toward a patient-specific multimodal eye model. *IEEE Trans Biomed Eng.* 2015;62:532–540.

31. Klein S, Staring M, Murphy K, Viergever MA, Pluim JPW. elastix: a toolbox for intensity-based medical image registration. *IEEE Trans Med Imaging.* 2010;29:196–205.

32. Shamonin D. Fast parallel image registration on CPU and GPU for diagnostic classification of Alzheimer's disease. *Front Neuroinform.* 2014;7:1–15.

33. Varian Medical Systems. Planning Reference Guide for Eclipse Ocular Proton Planning Eclipse Ocular Proton Planning. 2007;(September):1–286.

34. Koch NC, Newhauser WD. Development and verification of an analytical algorithm to predict absorbed dose distributions in ocular proton therapy using Monte Carlo simulations. *Phys Med Biol.* 2010;55:833–853.

35. Facilities P. 3 Beam delivery and properties. *J ICRU.* 2007;7:29–48.

36. Caujolle J-P, Paoli V, Chamorey E, et al. Local recurrence after uveal melanoma proton beam therapy: recurrence types and prognostic consequences. *Int J Radiat Oncol Biol Phys.* 2013;85:1218–1224.

37. Egger E, Zografos L, Schalenbourg A, et al. Eye retention after proton beam radiotherapy for uveal melanoma. *Int J Radiat Oncol Biol Phys.* 2003;55:867–880.

38. Sas-Korczynska B, Markiewicz A, Romanowska-Dixon B, Pluta E. Preliminary results of proton radiotherapy for choroidal melanoma - the Kraków experience. *Wspolczesna Onkol.* 2014;18:359–366.

39. Seibel I, Cordini D, Rehak M, et al. Local recurrence after primary proton beam therapy in uveal melanoma: risk factors, retreatment approaches, and outcome. *Am J Ophthalmol.* 2015;160:628–636.

40. Daftari IK, Aghaian E, O'Brien JM, Dillon W, Phillips TL. 3D MRI-based tumor delineation of ocular melanoma and its comparison with conventional techniques. *Med Phys.* 2005;32:3355–3362.

41. Ciller C, De Zanet SI, Rüegsegger MB, et al. Automatic segmentation of the eye in 3D magnetic resonance imaging: a novel statistical shape model for treatment planning of retinoblastoma. *Int J Radiat Oncol Biol Phys.* 2015;92:794–802.

42. Ciller C, De Zanet S, Kamnitsas K, et al. Multi-channel MRI segmentation of eye structures and tumors using patient-specific features. *PLoS One.* 2017;12:1–14.

43. Rüegsegger MB, Cuadra MB, Pica A, et al. Statistical modeling of the eye for multimodal treatment planning for external beam radiation therapy of intraocular tumors. *Int J Radiat Oncol Biol Phys.* 2012;84(4):e541–e547.

44. Goitein M, Miller T. Planning proton therapy of the eye. *Med Phys.* 1983;10:275–283.

45. Cirrone GAP, Cuttone G, Di Rosa F, Russo G, Salamone V. Monte Carlo validation of EYEPLAN proton therapy treatment planning. *Nucl Phys B - Proc Suppl.* 2007;172:273–276.

46. Daftari IK, Mishra KK, O'Brien JM, et al. Fundus image fusion in EYEPLAN software: an evaluation of a novel technique for ocular melanoma radiation treatment planning. *Med Phys.* 2010;37:5199–5207.

47. Marnitz S, Cordini D, Bendl R, et al. Proton therapy of uveal melanomas: intercomparison of MRI-based and conventional treatment planning. *Strahlentherapie und Onkol.* 2006;182:395–399.

48. Erb-Eigner K, Warmuth C, Taupitz M, Willerding G, Bertelmann E, Asbach P. Impact of magnetic field strength and receiver coil in ocular MRI: a phantom and patient study. *RoFo Fortschritte auf dem Gebiet der Rontgenstrahlen und der Bildgeb Verfahren.* 2013;185:830–837.

49. Lemke A-J, Hosten N, Wiegel T, et al. Intraocular metastases: differential diagnosis from uveal melanomas with high-resolution MRI using a surface coil. *Eur Radiol.* 2001;11:2593–2601.

50. de Jong MC, de Graaf P, Brisse HJ, et al. The potential of 3T high-resolution magnetic resonance imaging for diagnosis, staging, and follow-up of retinoblastoma. *Surv Ophthalmol.* 2015;60:346–355.

51. Char DH, Kroll S, Stone R d, Harrie R, Kerman B. Ultrasonographic measurement of uveal melanoma thickness: interobserver variability. *Br J Ophthalmol.* 1990;74:183–185.

52. Nürnberg D, Seibel I, Riechardt AI, et al. Multimodal imaging of the choroidal melanoma, with differential diagnosis, therapy (radiation planning) and follow-up. *Klin Monbl Augenheilkd.* 2018;235:1001–1012.

53. Thariat J, Maschi C, Lanteri S, et al. Dry eye syndrome after proton therapy of ocular melanomas. *Int J Radiat Oncol Biol Phys.* 2017;98:142–151.

54. Rethfeldt C, Fuchs H, Gardey KU. Dose distributions of a proton beam for eye tumor therapy: hybrid pencil-beam ray-tracing calculations. *Med Phys.* 2006;33:782–791.

55. Pfeiffer K, Bendl R. Real-time dose calculation and visualization for the. *Phys Med Biol.* 2001;46:671–686.

56. Breedveld S, Storchi PRM, Voet PWJ, Heijmen BJM. iCycle: Integrated, multicriterial beam angle, and profile optimization for generation of coplanar and noncoplanar IMRT plans. *Med Phys.* 2012;39:951–963.

57. Slopsema RL, Mamalui M, Zhao T, Yeung D, Malyapa R, Li Z. Dosimetric properties of a proton beamline dedicated to the treatment of ocular disease. *Med Phys.* 2013;41:011707.

58. Shin D, Yoo SH, Moon SH, Yoon M, Lee SB, Park SY. Eye tracking and gating system for proton therapy of orbital tumors. *Med Phys.* 2012;39:4265–4273.

59. Via R, Fassi A, Fattori G, et al. Optical eye tracking system for real-time noninvasive tumor localization in external beam radiotherapy. *Med Phys.* 2015;42:2194–2202.

60. Via R, Hennings F, Fattori G, et al. Noninvasive eye localization in ocular proton therapy through optical eye tracking: a proof of concept. *Med Phys.* 2018;45:2186–2194.

61. Via R, Pella A, Romanò F, et al. A platform for patient positioning and motion monitoring in ocular proton therapy with a non-dedicated beamline. *Phys Medica.* 2019;59:55–63.

62. Via R, Hennings F, Fattori G, et al. Technical Note: benchmarking automated eye tracking and human detection for motion monitoring in ocular proton therapy. *Med Phys.* 2020;47:2237–2241.

63. Denker A, Cordini D, Heufelder J, et al. Ion accelerator applications in medicine and cultural heritage. *Nucl Instrum Methods Phys Res Sect A.* 2007;580:457–461.

64. Carnicer A, Angellier G, Thariat J, Sauerwein W, Caujolle J p, Hérault J. Quantification of dose perturbations induced by external and internal accessories in ocular proton therapy and evaluation of their dosimetric impact. *Med Phys.* 2013;40:061708.

65. Newhauser WD, Koch NC, Fontenot JD, et al. Dosimetric impact of tantalum markers used in the treatment of uveal melanoma with proton beam therapy. *Phys Med Biol.* 2007;52:3979–3990.

66. La RV, Kacperek A, Royle G, Gibson A. Range verification for eye proton therapy based on proton-induced x-ray emissions from implanted metal markers. *Phys Med Biol.* 2014;59:2623–2638.

67. Daftari IK, Quivey JM, Chang JS, Mishra KK. Technical note: feasibility study of titanium markers in choroidal melanoma localization for proton beam radiation therapy: Feasibility. *Med Phys.* 2018;45:1036–1039.

SUPPORTING INFORMATION

Additional supporting information may be found online in the Supporting Information section at the end of the article.

Data S1. This document provides details on the ocular motility part and the in-house developed πDose proton eye dose algorithm.